Effects of including the adjoint sea ice rheology on estimating Arctic ocean-sea ice state

4 Guokun Lyu[1], Armin Koehl[2], Xinrong Wu[3], Meng Zhou[1,4], and Detlef Stammer[2]

5 [1]Shanghai Key Laboratory of Polar Life and Environment Sciences, School of Oceanography, Shanghai Jiao Tong
6 University, Shanghai, China

7 [2]Center for Earth System Research and Sustainability (CEN), University of Hamburg, Hamburg, Germany

8 [3]Key Laboratory of Marine Environmental Information Technology, National Marine Data and Information Service,
9 Tianjin, China

10 [4]MNR Key Laboratory for Polar Science, Polar Research Institute of China, Shanghai, China

12 *Correspondence to*: Guokun Lyu (guokun.lyu@sjtu.edu.cn)

13 **Abstract.** The adjoint assimilation method has been applied to coupled ocean and sea ice models for sensitivity studies
14 and Arctic state estimations. However, the accuracy of the adjoint model is degraded by simplifications of the adjoint
15 of the sea ice model, especially the adjoint sea ice rheologies. As part of ongoing developments in coupled ocean and
16 sea ice estimation systems, we incorporate and approximate the adjoint of viscous-plastic sea ice dynamics (adjoint-
17 VP) and compare it with the adjoint of a free drift sea ice dynamic (adjoint-FD) through assimilation experiments.
18 Using the adjoint-VP results in a further cost reduction of 7.9% in comparison to adjoint-FD, with noticeable
19 improvements in the ocean temperature over the open water and the intermediate layers of the Arctic Ocean. Adjoint-
20 VP more efficiently adjusts the uncertain model inputs more efficiently than does adjoint-FD by involving different
21 sea ice retreat processes. For instance, adjoint-FD melts the sea ice up to 1.0 m in the marginal seas from May to June
22 by over-adjusting air temperature (>8 °C); adjoint-VP reproduces the sea ice retreat with smaller adjustments to the
23 atmospheric state within their prior uncertainty range. These developments of the adjoint model here lay the foundation
24 for further improving Arctic Ocean and sea ice estimationS by comprehensively adjusting the initial conditions,
25 atmospheric forcings, and uncertain parameters of the model.

26
27

1 Introduction

The Arctic Ocean has experienced drastic changes, including rapidly declining sea ice (Comiso et al., 2008; Kwok, 2018), increased inventory of freshwater in the western Arctic (Proshutinsky et al., 2019), enhanced warm inflows from the Pacific Ocean (Woodgate et al., 2012) and the Atlantic Ocean (Polyakov et al., 2017; Quadfasel et al., 1991), and increased ocean primary productivity (AMAP, 2021), and has been migrating to a new state over the past decades. These changes potentially impact the climate and weather of the Northern Hemisphere (Ma et al., 2022; Overland et al., 2021).

In recent years, progress has been made in satellite techniques (e.g., Kaleschke et al., 2001; Spreen et al., 2008), in-situ observations (e.g., Toole et al., 2016; Morison et al., 2007; Polyakov et al., 2017; Proshutinsky et al., 2009; Schauer et al., 2008), and coupled ocean and sea ice models. However, the lack of extensive Arctic observations, especially direct observations of the state variables and fluxes through the water column, and the deficiencies in the coupled ocean and sea-ice model still obscure our understanding of the Arctic sea ice changes and extremes. Accurate predictions of sea ice are therefore limited (e.g., Yang et al., 2020).

To fill the gaps, research groups have applied data assimilation techniques to ingest available observations into coupled ocean and sea ice models. The resulting reanalyses are assumed to have higer accuracy since as the development of models and data assimilation methods progress and the observation numbers increase. Most of Arctic coupled ocean and sea ice data assimilation and operational forecasting systems use statistical methods such as optimal interpolation (e.g., Lindsay and Zhang, 2006) and ensemble Kalman filters (e.g., Mu et al., 2018; Sakov et al., 2012). The advantage of these statistical methods is that they ensure a local fit to available observations (within prior uncertainties of both model and observations). However, away from the observations and for the unobserved variables, these methods rely on the inaccurate spatial covariance of model states for interpolation. In addition, these algorithms can introduce artificial sink/source terms to the numerical models, violating the model physics.

Over recent decades, an adjoint method with a large assimilation window (years to decades) has been developed in the framework of Estimating the Circulation and Climate of the Ocean (ECCO, Heimbach et al., 2019; Stammer et al., 2002; Wunsch and Heimbach, 2007) to create dynamically consistent ocean reanalyses. This method iteratively minimises a cost function that measures the model-data "distance" by adjusting model uncertain inputs (control variables). The use of an adjoint model (adjoint of the tangent linear approximation of the nonlinear model) as a spatiotemporal interpolator distinguishes this method from the statistical methods. In addition, the adjoint method adjusts all uncertain inputs, including initial conditions, atmospheric forcing, and model parameters, rather than only the initial conditions as in statistical-based methods. The resulting reanalysis completely follows the model governing equations without having to consider artificial source/sink terms.

Despite the application of the coupled ocean and sea ice adjoint model in sensitivity studies (Heimbach et al., 2010; Kauker et al., 2009; Koldunov et al., 2013) and reanalyses (Fenty and Heimbach, 2013; Koldunov et al., 2017; Lyu et al., 2021b; Nguyen et al., 2021), we have to omit the adjoint of sea ice dynamics (Fenty et al., 2017; Nguyen et al., 2021) or simplify it to the adjoint of a free-drift sea ice model (Koldunov et al., 2017; Lyu et al., 2021b) to ensure numerical stability of the adjoint model. Toyoda et al. (2019) noted that further including the adjoint of sea ice rheology results in a much weaker evolution of sensitivity to sea ice velocity by O (10^2) in the central Arctic Ocean

65 than the adjoint of free-drift sea ice dynamics. It is expected that including the adjoint of sea ice rheology could better

66 project the model-data misfits to the control variables and potentially improve the quality of the reanalysis.

67 In this study, we incorporate and stabilise the adjoint of a viscous-plastic sea ice dynamic (Hibler, 1979; Zhang and

68 Hibler 1997), building on prior developments of the coupled Arctic ocean and sea ice model and assimilation system

69 (Koldunov et al., 2017; Lyu et al., 2021b). Using the unprecedented sea ice retreat process in 2012 as an example, we

70 evaluate the impacts of using the approximated adjoint of viscous-plastic sea ice dynamics on estimating the Arctic

71 ocean, sea ice, and sea-ice retreat processes.

72 The paper is organised as follows. In Section 2, we introduce the model configurations and assimilation

73 experiments. We assess the assimilation results in terms of the residual errors in Section 3. We examine adjustments

74 of the control variables in Section 4 and compare the sea ice retreat process in the assimilation runs in Section 5.

75 Section 6 summarises the results of this study and discusses the potential for a further development of global and

76 Arctic state and parameter estimation systems.

77

2 Model Configuration and Experiment Setups

2.1 The Coupled Ocean and Sea Ice Modelling and Assimilation System

80 The data assimilation system is based on the adjoint method in the ECCO framework, using the Massachusetts

81 Institute of Technology ocean general circulation model (MITgcm, Marshall et al., 1997) coupled with the zero-layer

82 dynamic-thermodynamic sea ice model of Hibler (1979). The sea ice dynamics are based on a viscous-plastic sea ice

83 rheology and are solved using a line successive over-relaxation algorithm (Zhang and Rothrock, 2000). The

84 thermodynamic sea ice model includes a prescribed sub-grid ice thickness distribution with 7 thickness categories. On

85 top of the ice, a diagnostic snow model is applied which modifies the heat flux and surface albedo, as in Zhang and

86 Rothrock (2000). The thermodynic-dynamic sea ice model simulates changes in sea ice drift (SID), sea ice

87 concentration (SIC), and mean sea ice thickness (in volume per unit area, mean SIT hereinafter). Losch et al. (2010)

88 reformulated the sea ice model on an Arakawa C grid to match the MITgcm oceanic grid and modified the model

89 codes to permit efficient and accurate automatic differentiation. The adjoint of the coupled ocean and sea ice model

90 is generated by the Transformation of Algorithms in FORTRAN (TAF, Giering and Kaminski, 1998).

91 The pan-Arctic model covers the Arctic Ocean north of the Bering Strait and the Atlantic Ocean at 44° N

92 (enclosed by black lines in Figure 1). In the horizontal direction, we use a curvilinear grid with a resolution of 12~15

93 km in the Arctic Ocean and ~18 km in the North Atlantic Ocean. In the vertical direction, the system has 50 z-levels

94 ranging from 10 m at the surface to 456 m in the deep ocean. The open boundaries are provided by a 16 km Atlantic-

95 Arctic Ocean simulation (Serra et al., 2010). At the ocean surface, we use the atmosphere state from the National

96 Centers for Environmental Prediction reanalysis 1 (NCEP-RA1, Kalnay et al., 1996) and bulk formulae (Large and

97 Yeager, 2004) to compute the momentum, heat, and freshwater fluxes. A virtual salt flux parameterisation simulates

98 the dilution and salinification of rainfall, evaporation, and river runoff. River runoff is applied near the river mouth

99 with seasonally varying discharge (Fekete et al., 2002). In addition, unresolved vertical mixing is parameterised using

100 the K-Profile scheme of Large et al. (1994). The background coefficients of vertical diffusion and viscosity are set to

101 10^{-5}m^{-2}s^{-1} and 5.6×10^{-4} m^{-2}s^{-1}, respectively. Biharmonic viscosity with a coefficient of 2.2×10^{11} m^{4}s^{-1} represents

102 unresolved sub-grid eddy mixing. The bottom topography is derived from ETOPO2 (Smith and Sandwell, 1997).
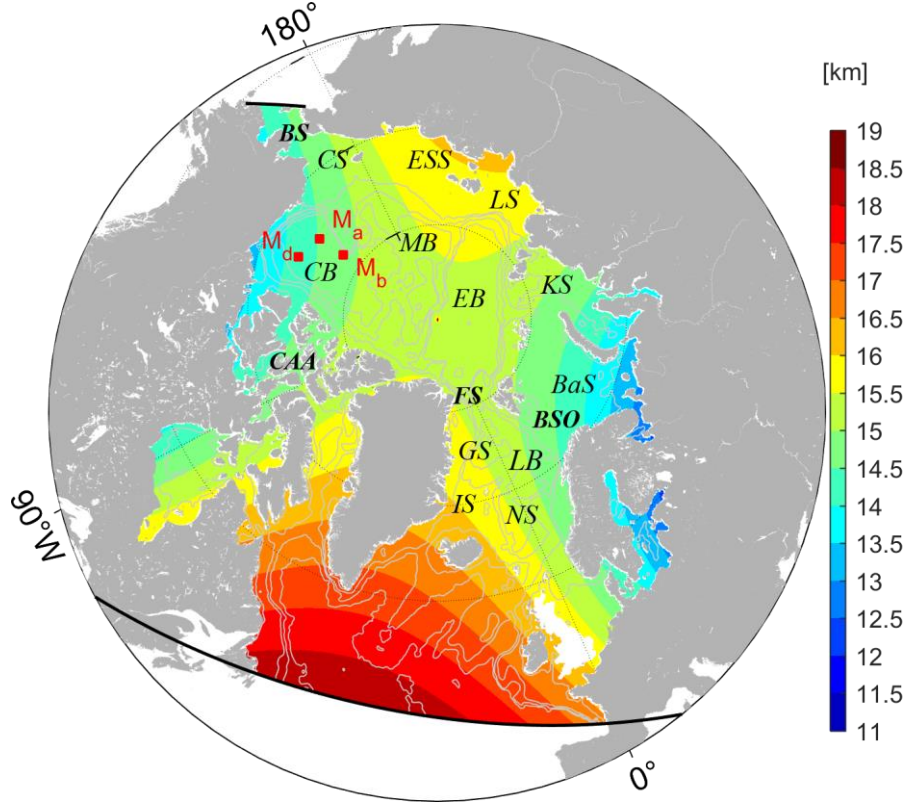
103
104 Figure 1. Map of the pan-Arctic regions showing the model domain (enclosed by the black lines) and horizontal
105 resolutions (shading). The red rectangles show the three moorings (M_a, M_b, M_d) from the Beaufort Gyre Exploration
106 Project (BGEP). Major basins and straits are labelled as follows: Canada Basin (*CB*), Makarov Basin (*MB*), Eurasian
107 Basin (*EB*), Chukchi Sea (*CS*), East Siberian Sea (*ESS*), Laptev Sea (*LS*), Kara Sea (*KS*), Barents Sea (*BaS*), Greenland
108 Sea (*GS*), Lofoten Basin (*LB*), Iceland Sea (*IS*), Norwegian Sea (*NS*), Bering Strait (*BS*), Fram Strait (*FS*), Barents
109 Sea Opening (*BSO*), and Canadian Arctic Archipelago (*CAA*).

110
111   The adjoint method brings the model simulation close to available observations by iteratively adjusting control

112 variables to minimise a quadric target function *J* (cost function hereafter):

113 $J(C_{ini}, C_{atm}(t)) = \sum_{t=1}^{T1}[y(t) - E(t)x(t)]^T R^{-2}[y(t) - E(t)x(t)] + C_{ini}^T P^{-2} C_{ini} + \sum_{t=0}^{T1} C_{atm}(t)^T Q_a^{-2} C_{atm}(t)$ (1).

114   On the right hand of Equation (1), the first term measures the model-data misfits weighted by the inverse error

115 covariance matrices (R^{-2}). The following section will introduce the available measurements and their uncertainties (*R*).

116 *y(t)* and *x(t)* are observations and the model state at time *t*, respectively. *E(t)* maps the model state *x(t)* to the

117 corresponding observations *y(t)*. The last two terms are background terms of the initial condition (C_{ini}) and the time-

118 varying atmospheric forcing ($C_{atm}(t)$) weighted by their inverse error covariance matrices (P^{-2} and Q_a^{-2}, respectively),

119 which penalise their adjustments and provide complete information on the controls. Following Lyu et al. (2021b),

120 prior uncertainties of the time-varying atmosphere state (Q_a) depend on geographic locations. They are computed as

121 the variance of the nonseasonal variability of the corresponding variables using NCEP-RA1.

122   For simplicity and the robust performance of this coupled data assimilation system, we choose the initial

123 conditions (C_{ini}), including temperature, salinity, mean SIT, SIC, and daily atmosphere state on the model grid ($C_{atm}(t)$),

124 which includes 10-m wind vectors, 2-m air temperature, 2-m specific humanity, precipitation, downwelling longwave,

125 and net shortwave radiation, as the control variables. In the future development of ocean and sea ice state estimation

126 systems, we further include the river runoff, the open boundary conditions, and model uncertain parameters as control

127 variables as in previous studies (e.g., Fenty and Heimbach, 2013; Liu et al., 2012). In this study, we use a one-year

128 assimilation window covering the year 2012, resulting in a total number of $\sim 2.7 \times 10^8$ control variables.

129 During the optimisation process, the adjoint of the coupled ocean-ice model is used to compute the gradients of

130 the cost function J to the control variables, and a quasi-Newton algorithm (Gilbert and Lemaréchal, 2006) is used to

131 iteratively reduce the cost function J. The optimisation process continues until the cost function cannot be further

132 reduced.

133 **2.2 Observations and Prior Uncertainties**

134 Both satellite and in situ measurements (Table 1) are used to constrain the model simulations. In addition, sea ice

135 draft measurements by up-looking sonar from the Beaufort Gyre Exploration Project (BGEP, see Figure 1 for the

136 locations) are used to independently validate the assimilation results.

137 Prior uncertainties are detailed in our previous Arctic synthesis study (Lyu et al., 2021b). Uncertainties in

138 temperature and salinity depend on the depth and are set to 0.6 ℃ and 0.3 PSU at the surface and 0.02 ℃ and 0.02

139 PSU in the deep ocean; SIC uncertainties consist of representation errors (15% within 50 km from the coastlines and

140 10% over the open water) and instrument errors. Because of higher errors in low SIC and lower errors over open water,

141 we modify the representation uncertainties by multiplicative factors of 0.85, 1.20, 1.10, and 1.00 for the observed SIC

142 ranges of 0.00, <15%, 15%–25%, and 0.25%, respectively.

143 SIT errors are provided by the datasets and interpolated to our model grid. Sea level anomaly (SLA) uncertainties

144 are set to 3.0 cm. SID uncertainties are dominated by representation errors and are set to 0.04 m/s. Sea surface

145 temperature (SST) uncertainties are provided by the datasets. In addition, we reduce the weight of the temperature and

146 salinity climatology (WOA18) cost components by factors of 20.0 and 10.0, respectively, to avoid overfitting to the

147 climatology.

148 **Table 1.** Assimilated measurements.

Date sets	Resolution	Number	Source
Sea level anomaly	7.0 km	7.6×10^5	Copernicus Marine Environment Monitoring Service, http://marine.copernicus.eu
Sea surface temperature	25.0 km	2.0×10^7	Remote Sensing System, http://www.remss.com/measurements/sea-surface-temperature/
T&S profiles	–	5.0×10^5	Good et al. (2013), https://www.metoffice.gov.uk/hadobs/en4/
Sea ice concentration	25.0 km	3.6×10^7	Kaleschke et al. (2001) and Spreen et al. (2008), SSMI (2011-2012), http://icdc.cen.uni-hamburg.de/1/daten/cryosphere.html
Sea ice thickness	25.0 km	8.9×10^6	Ricker et al. (2017), https://spaces.awi.de/pages/viewpage.action?pageId=291898639
Sea ice drift	62.5 km	5.8×10^5	Lavergne et al. (2019), https://osi-saf.eumetsat.int/products/osi-405-c
WOA18	1.0°	2.9×10^7	Zweng et al. (2018), https://www.nodc.noaa.gov/OC5/woa18/woa18data.html

149 **2.3 Viscos-Plastic Sea Ice Dynamics and Its Adjoint**

150 In the coupled ocean and sea ice model, the following equation governs sea ice drift:

$$\text{m}\frac{d\vec{u}}{dt} = -mf\vec{k} \times \vec{u} + \tau_{air} + \tau_{ocn} - \nabla\emptyset(0) + \nabla \cdot \sigma \tag{2}$$

151

152   where m is the sea ice mass and $\vec{u}$ is the sea ice motion vector; τ_{air} and τ_{ocn} are the wind and ocean drags,

153   respectively; $-\nabla\emptyset(0)$ is the tilt of the sea surface; and $\nabla \cdot \sigma$ is the divergence of the ice stress tensor σ_{ij}(i=1,2),

154   representing the internal forces of sea ice.

155   In the viscous-plastic rheology of Hibler (1979), the stress tensor σ_{ij} is related to the sea ice strain rate (ϵ_{ij}) and

156   strength (P):

$$\sigma_{ij} = 2\eta(\epsilon_{ij},P)\epsilon_{ij} + [\zeta(\epsilon_{ij},P) - \eta(\epsilon_{ij},P)]\epsilon_{kk}\delta_{ij} - \frac{P}{2}\delta_{ij} \tag{3}$$

157

158   where δ_{ij} is the Kronecker delta ($\delta_{ij} = 1$ if i=j, otherwise 0). η and ζ are the bulk and shear viscosities, expressed

159   as:

$$\zeta = \frac{P}{2\Delta_{reg}} \tag{4}$$

160

$$\eta = \frac{P}{2e^2\Delta_{reg}} \tag{5}$$

161

162   where

$$\Delta = [(\epsilon_{11}^2 + \epsilon_{22}^2)(1 + e^{-2}) + 2(1 - e^{-2})\epsilon_{11}\epsilon_{22} + 4e^{-2}\epsilon_{12}^2]^{\frac{1}{2}} \tag{6}$$

163

164   e is the ratio of normal stress to shear stress and is set to 2.0; $\Delta_{reg} = \max(\Delta, \Delta_{min})$ with Δ_{min} equals 1.0×10^{-10}. The

165   sea ice strain rate is computed as:

$$\epsilon_{ij} = \frac{1}{2}(\frac{\partial u_i}{\partial x_j} + \frac{\partial u_j}{\partial x_i}) \tag{7.}$$

166

167   The sea ice strength P depends on mean SIT (H) and SIC (C):

$$\text{P} = P^*H \cdot \exp(-C^* \cdot (1 - C)) \tag{8}$$

168

169   P^* and C^* are the ice compressive strength constant and ice strength decay constant and are set to 2.75×10^4 N m^{-2}

170   and -20.0, respectively.

171   The dependence of the internal force term ($\nabla \cdot \sigma$) on ice velocity is strongly nonlinear, leading to an unstable

172   adjoint of the coupled ocean-sea ice system. Therefore, previous studies (Koldunov et al., 2017; Lyu et al., 2021b)

173   used an adjoint of a free drift sea ice model (without an adjoint of $\nabla \cdot \sigma$). Toyoda et al. (2019) pointed out that the full

174   adjoint of Equation (2) can be stabilised by eliminating the dependence of bulk and shear viscosities on the strain rate

175   (ϵ_{ij}).

176   Following the study of Toyoda et al. (2019), we eliminate the dependence of bulk and shear viscosities on ϵ_{ij} in

177   the adjoint of Equation (2). In addition, we note that there are still strong sensitivities that hamper the convergence of

178   optimization. We set the adjoint sensitivities of ice velocity to zero if the local sensitivity is 50 times larger than the

179   global mean of their absolute values. In addition, we also modify the adjoint model in the following ways to ensure

180   the stability of the adjoint model over a one-year assimilation window:

181   1) Disable the K-profile mixing parameterisation scheme;

182   2) Increase the Laplacian diffusivity of heat and salinity to 500 m^2 s^{-1} and lateral eddy viscosity to 10,000 m^2 s^{-}

183   ^{1};

184   3) Apply a spatial filter to sensitivity variables calculated in the adjoint of the thermodynamic sea ice model

185   (see APPENDIX in Lyu et al. (2021b) for details).

186   Since the sea ice dynamic model is solved using an iterative line successive over-relaxation solver, we note that

187   the approximated adjoint of the viscous-plastic sea ice dynamic (adjoint-VP) requires ~1.2 times the computational

188   cost of using the adjoint of a free-drift sea ice model (adjoint-FD).

189
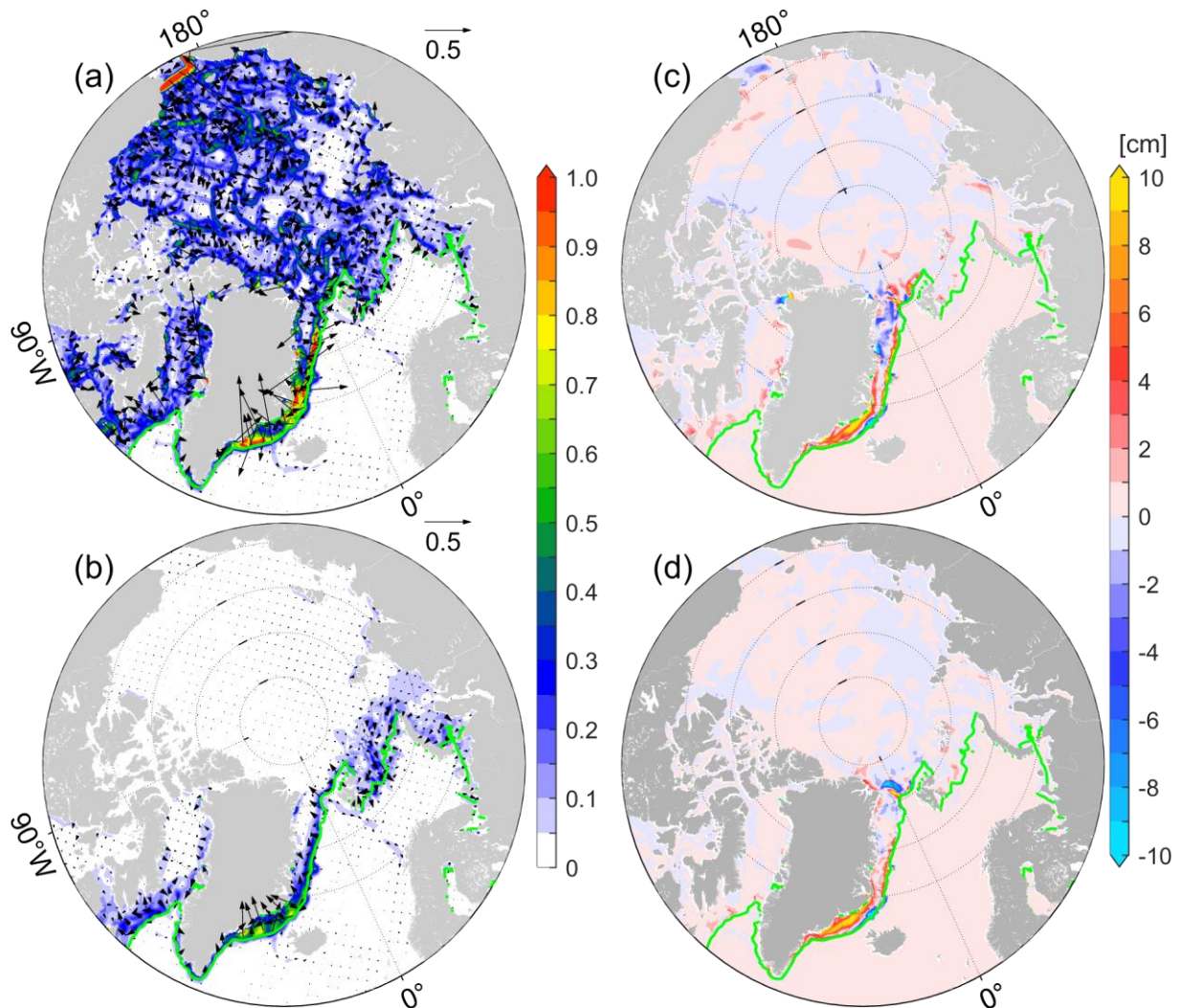
190

191   Figure 2. Sensitivities of total sea ice volume to wind vectors (in $0.1 \times km^3$ $(m\ s^{-1})^{-1}$, shadings represents amplitudes)
192   using the adjoint of (a) a free-drift sea ice dynamic and (b) viscous-plastic sea ice dynamics with modifications in
193   Section 2.3. Panels (c)-(d) show the mean SIT changes by perturbing the wind with the corresponding adjoint
194   sensitivities multiplied by a factor of 10^{-8}. The green lines are the sea ice extents (SIEs, 15% SIC) in January 2012.

195

196   Based on adjoint-FD and adjoint-VP, we compute the sensitivities of domain-integrated sea ice volume with

197   respect to the atmospheric forcings and the initial conditions over the period of January 1 to January 31, 2012. As

198   reported by Toyoda et al. (2019), adjoint-FD shows much stronger sensitivities to wind than does adjoint-VP (Figure

199   2a, b) in the central Arctic Ocean. Along the sea ice marginals (SIMs) of the Atlantic sectors, adjoint-VP reveals that

200   the towards-ice wind anomalies increase total sea ice (Figure 2b) since they prevent ice from drifting to the warm

Atlantic water. However, adjoint-FD shows strong sensitivities along the SIMs of the Atlantic sectors, but both towards-ice and off-ice wind anomalies appear (Figure 2a), potentially resulting in ice convergence.

Furthermore, we add daily wind perturbations, computed by scaling the adjoint sensitivities (Figure 2a, b) so that the maximum perturbations are 1.0 m s^{-1}, to the 6-hourly wind from NCEP-RA1 and examine their impacts on mean SIT changes. As expected, mean SIT changes are mainly along the SIMs in the Atlantic sectors (Figure 2c, d), and wind perturbations from adjoint-FD reduces mean SIT northeast of Greenland (Figure 2c). In the central Arctic Ocean with compact ice, the internal forces $\nabla \cdot \sigma$ oppose the impacts of wind perturbations. Therefore, despite the strong adjoint sensitivities to the wind in adjoint-FD, we note that the resulting wind perturbations only slightly change the mean SIT (Figure 2c), which is comparable to that in adjoint-VP (Figure 2d).

In addition to overestimating the sensitivities to wind, adjoint-FD may degrade the usefulness of the adjoint sensitivities in optimisation. Therefore, we perform two assimilation experiments to comprehensively evaluate the impacts of including the approximate adjoint of sea ice rheology on ocean and sea ice estimations.

3 Model-Data Misfit Reductions and Residuals

3.1 Evaluation of the Optimisation

In this study, we consider iteration 0 the control run. In adjoint-FD and adjoint-VP, the optimisations stall at iterations 13 and 32, and the further cost function reductions at the last two successive iterations are 0.7% and 0.2% of the total cost, respectively. After the optimisations, the total cost and norms of the gradients are reduced by 32.3% and 59.2% , respectively, in adjoint-FD and by 40.2% and 89.3%, respectively, in adjoint-VP.

Table 2. Normalised costs and reductions in the two optimisation runs.

Cost constituent	**Control run**	**Adjoint-FD**		**Adjoint_VP**	
	Normalised cost (%)	Normalised cost (%)	Percentage reduction (%)	Normalised cost (%)	Percentage reduction (%)
J_{Total}	100	67.7	32.3	59.8	40.2
J_{SLA}	2.2	2.1	4.6	2.1	4.6
J_{SST}	25.3	15.4	39.1	12.9	49.0
$J_{profile\_T}$	6.9	6.5	5.8	4.3	37.7
$J_{profile\_S}$	5.8	5.9	-1.7	4.5	22.4
J_{SIC}	39.7	18.4	53.7	18.1	54.4
J_{SIT}	3.6	3.1	13.9	2.7	25.0
J_{SID}	4.5	4.4	2.2	4.3	4.4
J_{WOA_T}	6.6	6.6	0.0	6.2	6.1
J_{WOA_S}	5.4	5.3	1.9	4.7	13.0

Of the individual cost constituents (Table 2), satellite-observed SST (J_{SST}) and SIC (J_{SIC}) contribute ~25.3% and 39.7% of the total cost, respectively, which are significantly reduced after optimisation. The costs of the temperature ($J_{profile\_T}$) and salinity ($J_{profile\_S}$) profiles are also considerably reduced, especially in the adjoint-VP. The rest of the cost constituents are also slightly reduced. Overall, including the adjoint of sea ice rheology further reduces the total cost by 7.9% and the individual cost constituents, especially J_{sst}, $J_{profile\_T}$ and $J_{profile\_S}$. Based on iterations 0, and 13 in adjoint-FD, and 32 in adjoint-VP of the optimisation, we will focus on the sea ice state and ocean temperature to evaluate the impacts of using this approximate adjoint of sea ice rheology.

3.2 Sea Ice State

3.2.1 Residual Errors of SIC and SIT

Satellite visual, infrared, and microwave technologies have been applied to monitor SIC with high frequencies and quality, which is of high priority in global and Arctic-focused synthesis (Chevallier et al., 2017; Uotila et al., 2019). Previous studies (Fenty and Heimbach, 2013; Lyu et al., 2021a; Lyu et al., 2021b) indicated that SIC could be significantly improved by slightly adjusting the atmospheric forcings. Here, we explore the residual errors in the optimisation runs.
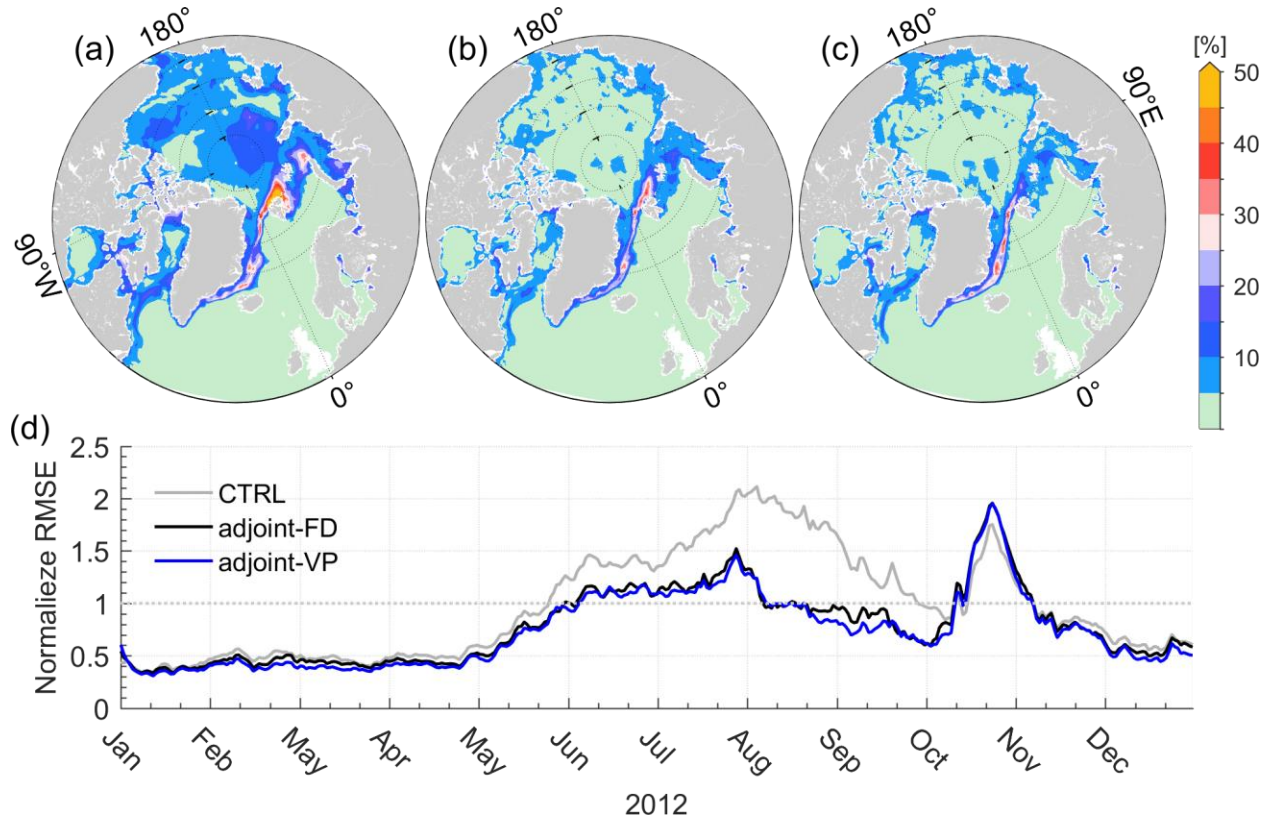
Figure 3. Root mean square errors (RMSEs) of SIC between the satellite measurements and (a) the control run, (b) adjoint-FD, and (c) adjoint-VP averaged over 2012. Panel (d) shows the temporal variations in RMSEs normalised by prior uncertainties in the three simulations averaged over the sea ice-covered regions.

The root mean square errors (RMSEs) of SIC averaged over 2012 (Figure 3a-c) and normalised by the prior errors and averaged over the model domain (Figure 3d) show the geographical distribution and temporal evolution of SIC errors, respectively. The normalised RMSEs in Figure 3d should be close to 1.0 if the optimisation found a model simulation consistent with the observations and the prior uncertainties.

The control run (Figure 3a) shows pronounced RMSEs in the Beaufort Gyre (~15%), the central Eurasian Basin (15%~20%), the marginal seas (15%~20%), and SIMs of the Atlantic sector (30%-50%). The normalised RMSEs reveal that SIC errors remain small (~0.5) in the winter time (Figure 3d), indicating that the control run and the satellite SIC measurements match well, but they grow quickly from May-September when the sea ice melts (Figure 3d).

249 Normalised RMSEs up to 1.5 are observed in October but quickly drop in November (Figure 3d). Therefore, SIC

250 errors are significant during the melting and refreezing periods (from May to November).

251   Both assimilation experiments reduce the SIC errors to less than 5% in the central Arctic Ocean and 10% in the

252 marginal seas. SIC errors of up to 20% persist in the Atlantic sector, where sea ice shows strong nonlinearity and the

253 tangent linear model can capture only part of the sea ice changes (APPENDIX B in Lyu et al., 2021a). Normalised

254 SIC errors from May to September are also reduced to close to 1.0 by assimilation of the daily SIC observations

255 (Figure 3d). However, SIC errors in October remain significant (Figure 3d) since the observed sea ice recovers much

256 faster than in the control run and the two assimilation runs (not shown here). This delayed sea ice recovery in the

257 model may be related to model uncertain parameters, such as the threshold thickness between thin and thick ice, which

258 determines the initial sea ice thickness formed in open water.
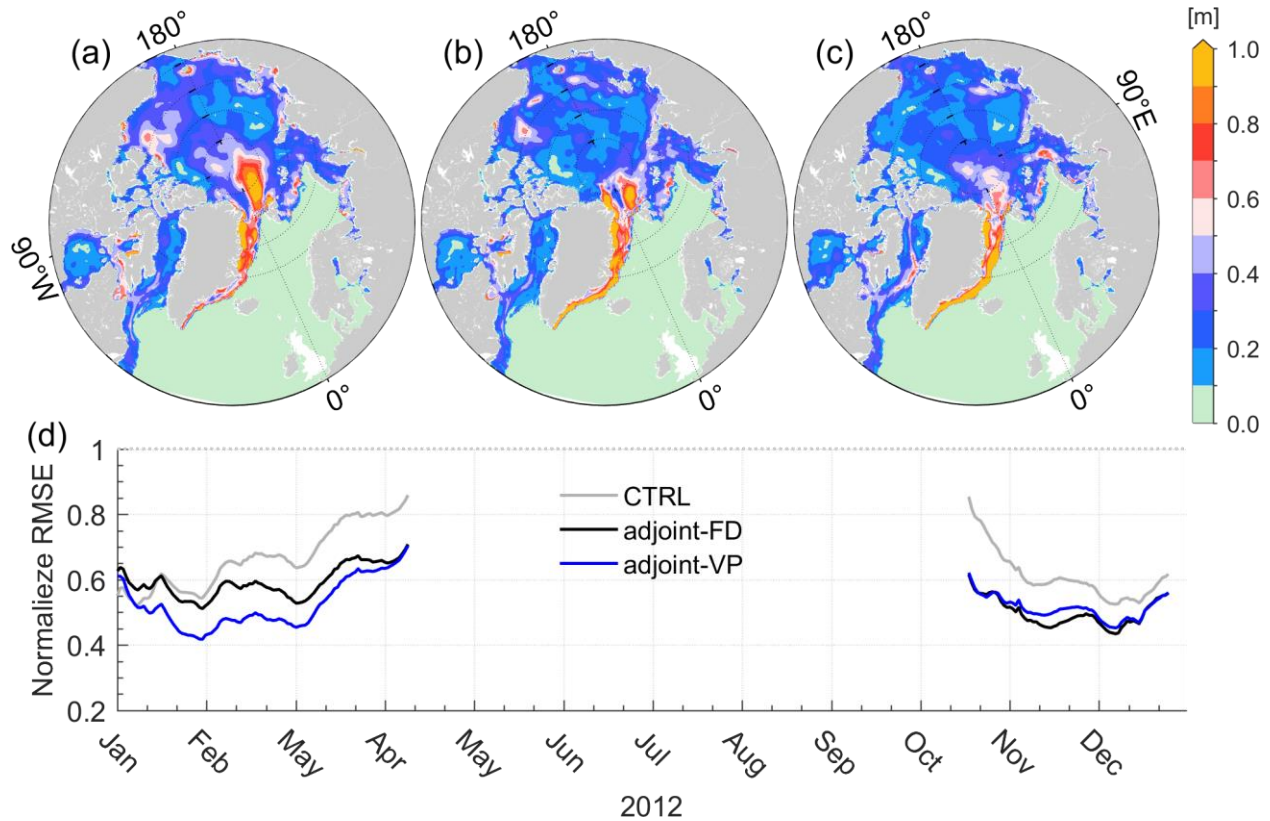
260 Figure 4. Root mean square errors (RMSEs) of SIT between the satellite measurements and (a) the control run, (b)
261 adjoint-FD, and (c) adjoint-VP averaged over 2012. Panel (d) shows the temporal variations in RMSEs normalised by
262 prior uncertainties in the three simulations averaged over the sea ice-covered regions.

264   The control run shows SIT errors of up to 1.0 m in regions north and south of the Fram Strait and approximately

265 0.4~0.7 m in the Beaufort Gyre. In the Beaufort Gyre, the SIT errors are reduced to less than 0.3 m in adjoint-VP

266 (Figure 4c) and approximately 0.3-0.5 m in adjoint-FD (Figure 4b). Similar to the SIC errors, SIT errors of up to 1.0

267 m remain along the East Greenland Current, which seems to increase in the two assimilation experiments. The

268 temporal evolutions of normalised RMSEs show that the SIT errors grow quickly from February to April (Figure 4d).

269 Both assimilation experiments reduce the SIT errors, especially in adjoint-VP from January to April (Figure 4d).

270   However, the normalised RMSEs of SIT averaged over the model domain remain smaller than 1.0 and seem to grow

271   during the melting season. More accurate SIT observations (e.g., half of the uncertainties) and SIT observations during

272   the melting season are required to facilitate a significant impact on the model simulation.

3.2.2 BGEP Mooring Measurements

274   Independent sea ice draft measured by up-looking-sonar (ULS) on the BGEP moorings (M_a, M_b, and M_d in

275   Figure 1) is used to validate the simulated sea ice draft. The simulated snow depth (d_{snow}) and SIT (d_{SIT}) are used to

276   compute the sea ice draft following the methods of Tilling et al. (2018):

$$\text{draft} = \frac{\rho_i \times d_{SIT} + \rho_s \times d_{snow}}{\rho_w} \tag{9}$$

278   where ρ_i, ρ_s, and ρ_w are the densities of the sea ice, snow, and water, respectively, and are set to 910.0, 330.0, and

279   1027.5 kg m^{-3} , respectively, as in our model.
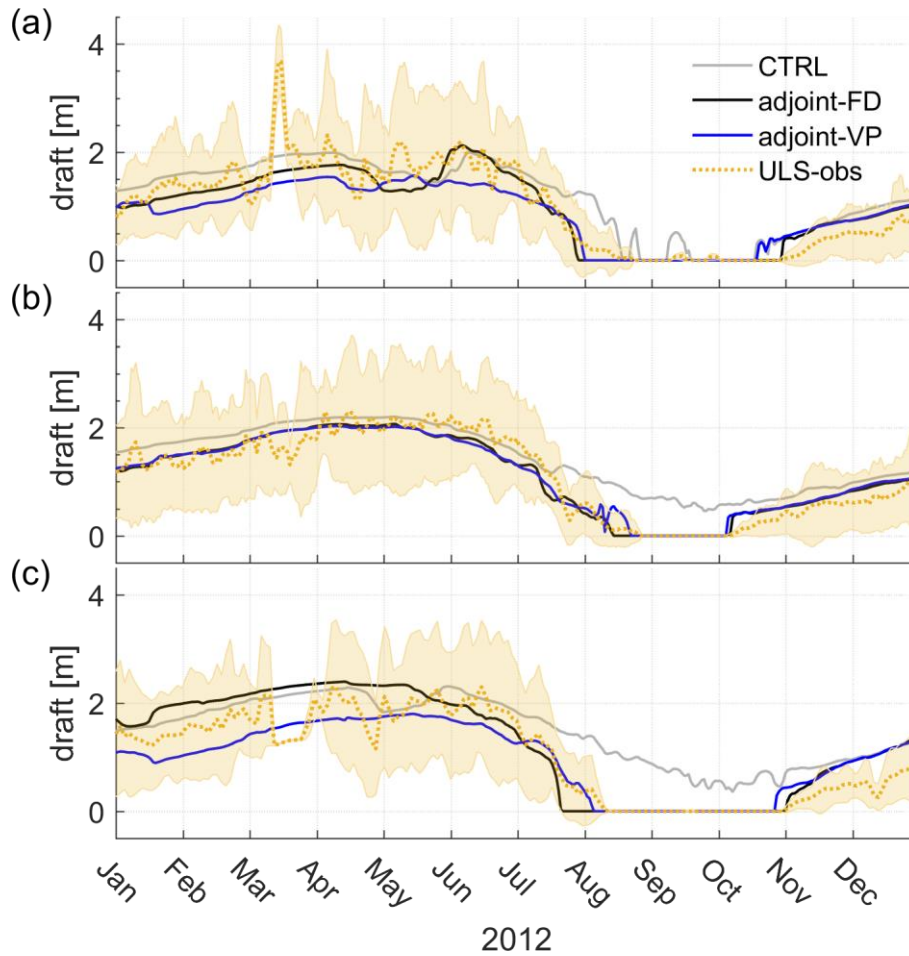
281   Figure 5. Daily time series of the sea ice draft (dotted yellow lines) and the daily standard deviation (shadings) at the
282   mooring locations (a) M_a, (b), M_b, and (c) M_d compared with the control run and the two assimilation runs (see the
283   legend) throughout the year 2012. ULS-observed sea ice drafts are smoothed with a 5-day running average.

285   The ULS measurements depict stronger daily to sub-monthly sea ice draft variability than do the model

286   simulations, which may be related to ice floe motions. The control run simulates a delayed ice disappearance process

287 in M_a (Figure 5a) and fails to reproduce the sea ice disappearance processes in M_b (Figure 5b) and M_d (Figure 5c) from

288 August to October. After optimisation, adjoint-VP and adjoint-FD reproduce the sea ice melting and refreezing

289 processes well, although errors of up to 0.5 m remain from January to June. Overall, the two assimilation runs

290 reproduce the local sea ice retreat and recovery process well.

291

292 **3.3 Ocean Temperature**

293 Ocean temperature changes are closely related to sea ice changes. Adjoint-VP introduces more pronounced ocean

294 temperature changes than does adjoint-FD. Here, we explore ocean temperature changes after assimilation.
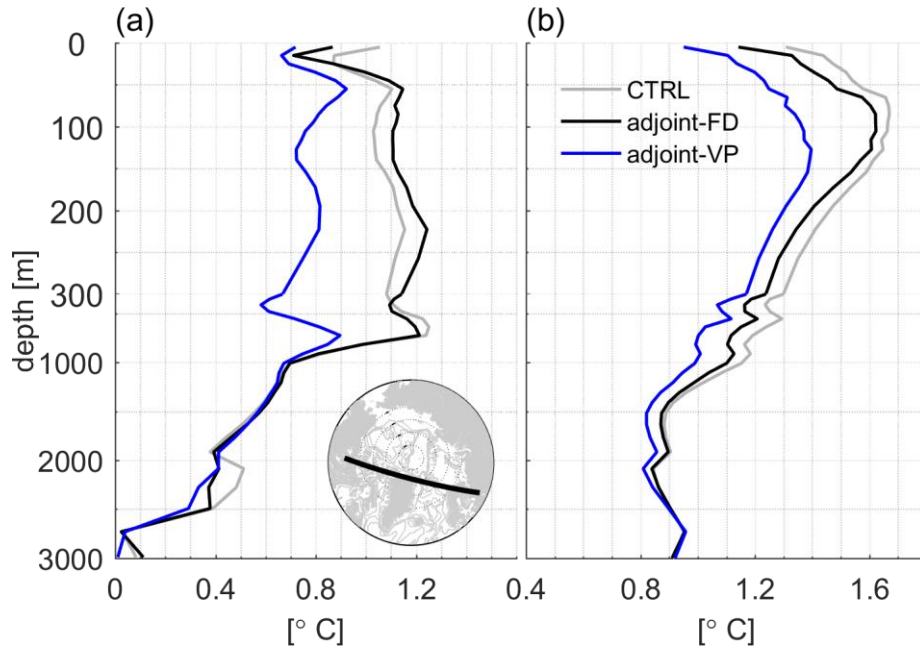
295
296
297 Figure 6. RMSEs of potential temperature (a) in the Arctic Ocean and (b) the North Atlantic Ocean in the three runs.
298 The Arctic Ocean and the North Atlantic Ocean are separated by the black lines in the bottom subplot.
299

300 In the Arctic Ocean, adjoint-FD reduces temperature errors only over the top 20 m, while adjoint-VP reduces

301 temperature errors up to 0.4 °C over the top 1000 m (Figure 6a). In the North Atlantic Ocean, adjoint-VP results a in

302 more pronounced RMSEs reduction up to 0.3 °C than adjoint-FD (Figure 6b).

303 Relative temperature error reductions over the top 50 m reveal an overall improvement in temperature with

304 occasional degradation (Figure 7a, b). Adjoint-VP results in a more significant error reduction than does adjoint-FD

305 in the North Atlantic Ocean (Figure 7a, b). In the southern Beaufort Gyre, the Laptev and Kara seas, and north of

306 Svalbard, both adjoint-VP and adjoint-FD increase the ocean temperature (over 50 m) since the two optimisation runs

307 reproduce the early retreat of the sea ice well, allowing more solar heating of the open water. In the North Atlantic

308 Ocean, adjoint-VP achieves more considerable temperature changes than does adjoint-FD both over the top 50 m

309 (Figure 7c, d) and from 50 m-700 m (Figure 7e, f). In the Arctic Ocean, adjoint-VP further introduces negative

310 temperature corrections between 50 and 700 m (Figure 7f), especially near the profile locations (see dots in Figure

311 7b).
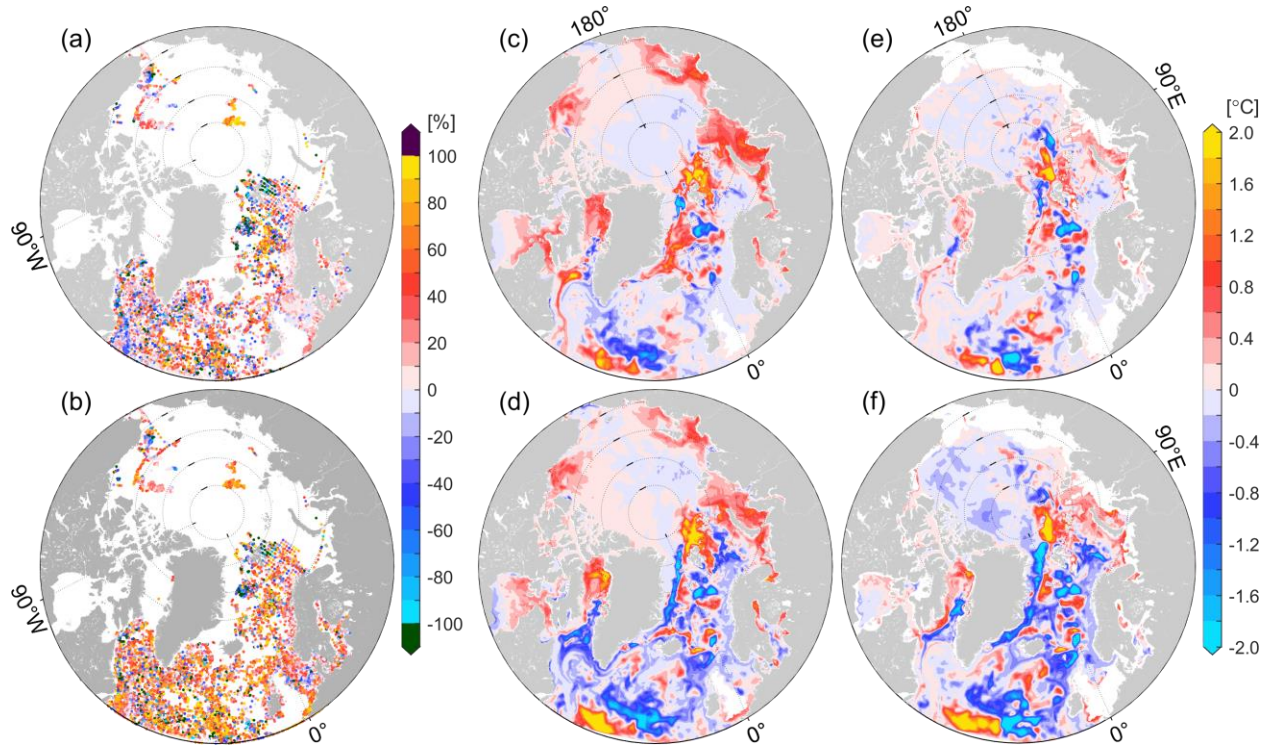
Figure 7. Relative temperature error reduction ($-\frac{|T_{opti}-T_{obs}|-|T_{ctrl}-T_{obs}|}{|T_{ctrl}-T_{obs}|} \times 100\%$) over the top 50 m at the profile locations in (a) adjoint-FD and (b) adjoint-VP. Values >100% indicate over-adjustment. Panels (c) and (d) show the temperature differences of adjoint-FD and adjoint-VP to the control run averaged over the top 50 m, respectively. Panels (e) and (f) are the same as Panels (c) and (d), but for the 50-700 m layers.

In summary, adjoint-FD and adjoint-VP reproduce the SIC variations well in the Arctic Ocean, which further reduces ocean temperature errors in the top layer by improving the atmosphere-ocean heat flux. Adjoint-VP achieves more significant corrections to the ocean temperature over the open water and in the intermediate layer of the Arctic Ocean than does adjoint-FD.

4 Adjustment of the Control Variables

The adjoint models project the model-data misfits onto the gradient of the objective function with respect to all control variables simultaneously, which is used by the optimisation algorithm to adjust the control variables. In this section, we compare adjustments of the control variables in the adjoint-FD and adjoint-VP and evaluate contributions of individual adjustments of the control variables on the cost function reduction. We also compare the adjustments of the control variables in adjoint-FD and adjoint-VP with differences between ERA5 (Hersbach et al., 2020) and NCEP-RA1 reanalyses.

Among all the control variables, wind vectors and 2-m air temperature are considerably adjusted in adjoint-FD and adjoint-VP but also show significant differences. In addition, adjoint-VP induces more pronounced adjustments of the initital temperature and salinity than does adjoint-FD (not shown here). Here, we concentrate on the adjustments of wind vectors and the 2-m air temperature.
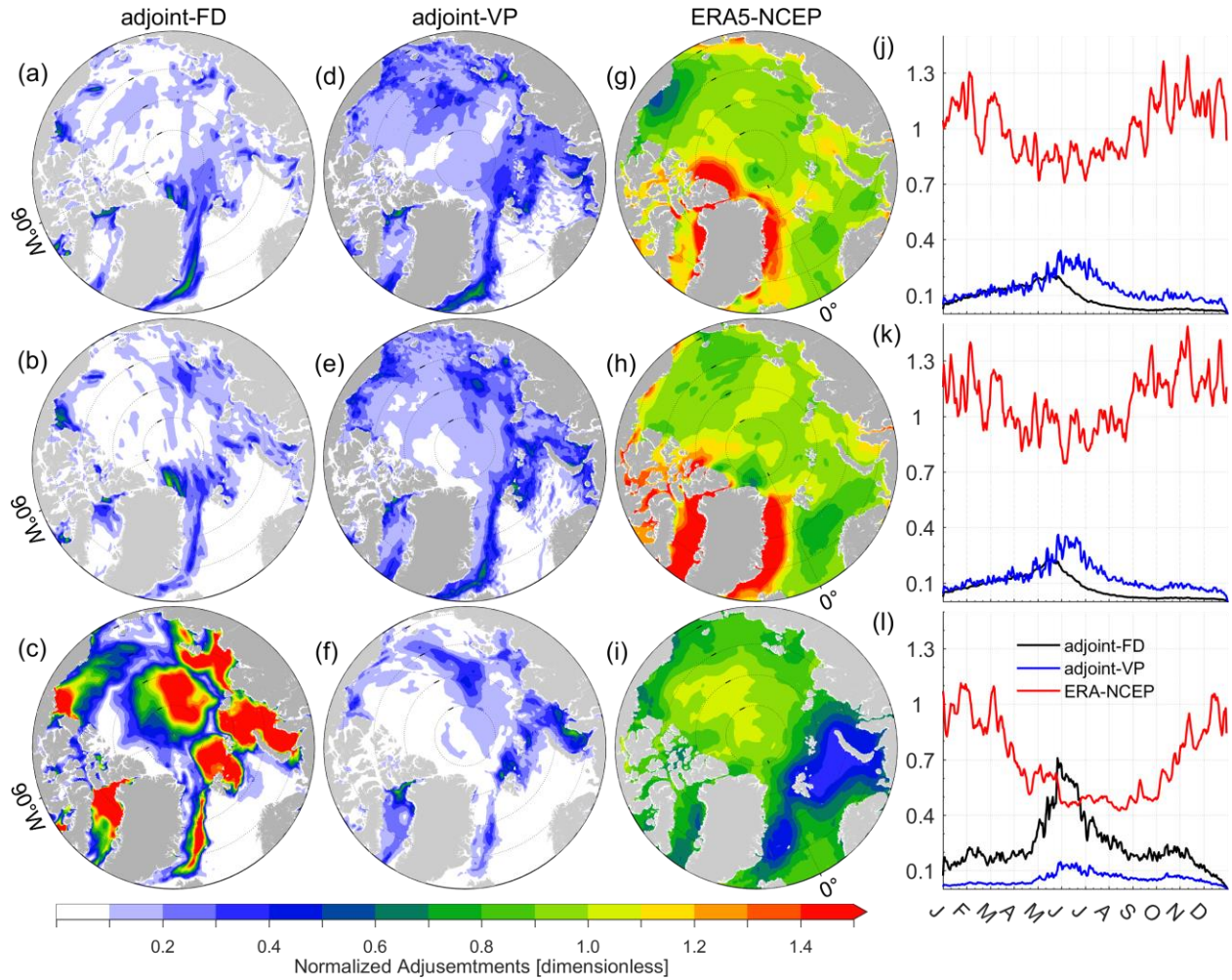
Figure 8. Root mean square (RMS) of the adjustments of the (a) wind *u*-component, (b) wind *v*-component, and (c) 2-m air temperature normalised by their prior uncertainties (dimensionless) in adjoint-FD and averaged over 2012. Panels (d)-(f) are similar to (a)-(c) but for adjoint-VP. Panels (g)-(i) show the normalised RMS of differences in the (g) wind *u*-component, (h) wind *v*-component, and (i) 2-m air temperature between ERA5 and NCEP-RA1 reanalyses (normalised by prior uncertainties in assimilation experiments). Panels (j)-(l) are the area averages of the normalised RMS of adjustments (differences) of the wind *u*-component, wind *v*-component, and 2-m air temperature (dimensionless) in adjoint-FD and adjoint-VP (ERA5-NCEP).

Figure 8 shows the root mean square (RMS) of the adjustments of the wind vectors and 2-m air temperature normalised by their prior uncertainties. The normalised RMS of the adjustments of the control variables should be smaller than 1.0 if the adjustments are within their prior uncertainties. Adjoint-FD slightly adjusts the wind vectors (with the normalised RMS of the adjustments being smaller than 0.4, Figure 8a, b), but the 2-m air temperature is significantly adjusted (with the normalised RMS of adjustments being greater than 1.5, Figure 8c). In adjoint-VP, the wind vectors and 2-m air temperature are slightly adjusted (Figure 8d-f) with their normalised RMS of adjustments being smaller than 0.3. In addition to the different amplitudes of the adjustments, the maximum adjustments of the wind vectors appear in June in adjoint-VP but in May in adjoint-FD (Figure 8j, k). Throughourt 2012, the 2-m air temperature is adjusted more prominently in adjoint-FD than in adjoint-VP (Figure 8l).

We note that the adjustments of the three atmosphere state variables in Figure 8a-f resemble the SIC (Figure 3a) and SIT (Figure 4a) error patterns, indicating that these adjustments are mostly determined by sea ice state errors that are projected on the control variables by the adjoint models rather than the background terms (the second and third terms on the right hand side of Equation (1)). Excluding the adjoint of sea ice rheology (adjoint-FD) results in over-adjustments of 2-m air temperature. With an approximated adjoint of sea ice rheology (adjoint-VP), we reduce the model-data misfits by slightly adjusting the control variables.

Using the new generation ERA5 reanalysis, we further compare the ERA5-NCEP differences against the adjustments of the atmosphere state variables in terms of their spatial patterns and temporal variability. The purpose of this comparison is twofold: 1) it further justifies the rationale of the adjustment amplitudes, and 2) it examines whether the adjustments reflect the differences between the old generation NCEP-RA1 reanalysis and the new generation ERA5 reanalysis. For the wind vectors, the normalised RMS differences between the ERA5 and NCEP-RA1 reanalyses (Figure 8g, h) are much larger than the wind vector adjustments in adjoint-FD (Figure 8a, b) and adjoint-VP (Figure 8d, e). For the 2-m air temperature, the normalised ERA5-NCEP differences (>1.0, Figure 8i) are much larger than the normalised adjustments in adjoint-VP (<0.3, Figure 8f) but smaller than the normalised adjustments in adjoint-FD (>1.5, Figure 8c) in the Kara Sea, the Laptev Sea, the southern Beaufort Sea, the Eurasian Basin and the Makarov Basin. It is evident that the 2-m air temperature adjustments in adjoint-FD are too large. Averaged over the model domain and throughout 2012, the ERA5-NCEP differences are much larger than the adjustments (Figure 8j-l) in the two assimilation runs. In addition, the adjustments are larger from May to August than from September to April, while the ERA5-NCEP differences are larger in the winter season than in the summer season (Figure 8j-l). The comparisons confirm that the 2-m air-temperature is over-adjusted in adjoint-FD, especially from May to July (Figure 8l). The adjustments of wind vectors and 2-m air temperature do not resemble the ERA5-NCEP differences, indicating that the model-data differences cannot be fully fixed by replacing the old generation NCEP-RA1 reanalysis with the new generation ERA5 reanalysis.

Table 3. Contributions of the adjustments of 2-m air temperature, wind vectors, initial temperature and salinity (Initial T&S), and the remaining control variables (including initial mean SIT and SIC, 2-m specific humanity, precipitation, downwelling longwave, and net shortwave radiation) on the total cost reduction, SIC, SST, and temperature profiles in the two optimisation runs.

	Adjoint-FD (%)				Adjoint-VP (%)			
	2-m air temperature	Wind vectors	Initial T & S	Remaining variables	2-m air temperature	wind	Initial T & S	Remaining variables
J_{total}	29.0	17.5	6.0	3.0	5.3	52.6	25.1	5.0
J_{SIC}	25.5	19.8	2.4	1.2	4.5	64.9	10.1	2.4
J_{SST}	41.0	8.6	10.1	5.5	8.4	47.4	29.6	6.4
J_{prof_T}	3.9	4.9	4.3	4.3	4.4	40.9	182.0	7.9

By replacing the adjusted initial temperature and salinity, wind vectors, 2-m air temperature, and the remaining control variables with NCEP-RA1 datasets, we integrate the model and estimate the contributions of these variables to the total cost reductions and individual components. Table 3 summarises contribution of individual control variables to the total cost reductions and cost components of SIC, SST, and temperature profiles.

384   The small contributions of the adjustments of the remaining control variables ("Remaining variables" in Table 3)

385   to the cost function reductions in adjoint-FD and adjoint-VP highlight the importance of simultaneous adjustments of

386   the initial temperature and salinity, wind vectors and 2-m air temperature. In adjoint-FD, the adjustments of the 2-m

387   air temperature and wind vectors dominate the cost function reduction, especially the SIC components. In contrast,

388   adjoint-VP relies more on the adjustments of the wind vectors and the initial temperature and salinity. Besides, the

389   more pronounced ocean temperature improvements (see Figure 7) in adjoint-VP are mostly attributed to the

390   adjustments in the initial temperature and salinity (Table 3).

391   Overall, Adjoint-FD attributes more of the model-data misfits to the 2-m air temperature than does the adjoint-VP,

392   resulting in over-adjustments of the 2-m air temperature. By using an approximated adjoint of the sea ice rheology

393   (adjoint-VP), we reduce the model-data misfit by slightly adjusting the control variables. This leads to the conclusion

394   that the large 2-m air temperature adjustments in adjoint-FD is likely an overcompensation for wind errors that cannot

395   be appropriately corrected because of large errors in the respective cost function gradients.

5 The Impacts on Sea Ice Retreat Processes

397   A unique characteristic of the adjoint-based reanalysis is that its physical processes are described by the

398   governing equations of the model, allowing us to quantify the sea ice loss and the contributions of the sea ice dynamics

399   and sea ice-ocean-atmosphere fluxes through a closed budget analysis. In this section, we explore and compare the

400   mean SIT changes based on the model governing equation:

401
$$\frac{dh}{dt} = -\nabla \cdot (\vec{u}h) + F_{oi} + F_{ai} + F_{res} \qquad (10).$$

402   The mean SIT tendency $\frac{dh}{dt}$ is dominated by the sea ice advective flux ($-\nabla \cdot (\vec{u}h)$), ocean-sea ice heat flux (F_{oi})

403   at the sea ice bottom, atmosphere-sea ice flux (F_{ai}) at the sea ice surface, and a residual term (F_{res}) including a snow

404   flooding effect and a source term to correct negative mean SIT to zero. F_{oi} depends on ocean temperature difference

405   from freezing temperature (Maykut and Mcphee, 1995) and F_{ai} consists of the radiation and turbulence fluxes over

406   the sea ice surface. The contributions of the residual terms are small and therefore we do not show them in the analysis

407   below.

408   Integrate the mean SIT over the Arctic Ocean (see Figure 9 for the locations), we derive Arctic sea ice volume

409   (SIV) changes. As shown in Figure 9a, the two assimilation runs change the total Arctic SIV changes in different ways.

410   Adjoint-VP reduces the Arctic SIV by reducing the initial Arctic SIV and changing the SIV tendency from May to

411   August. By September, adjoint-VP simulates more sea ice than the control run. Adjoint-FD slightly increases the

412   initial SIV, and the signals are invisible by February 2012. From May to July, adjoint-FD shows a stronger sea ice

413   melting process than the control run and adjoint-VP. By September, adjoint-FD simulates the most SIV among the

414   three simulations.

415   Based on Equation (10), we further compare SIV tendencies and the budget terms in the two assimilation runs

416   (Figure 9b). The two assimilation runs reveal that the seasonal SIV changes are dominated by F_{ai} (magenta lines in

417   Figure 9b). Throughout the year, the ocean melts the sea ice from the bottom (blue lines in Figure 9b) and net sea ice

418   transport also reduces the Arctic sea ice (green lines in Figure 9b). However, we note that a much stronger sea ice loss

419   process occurs from May 20 to June 15 in adjoint-FD (up to -193.0 km^3 day^{-1}) than in adjoint-VP (up to -125.0 km^3

420   day^{-1}), which is mainly attributed to F_{ai} anomalies (magenta lines in Figure 9b).

421
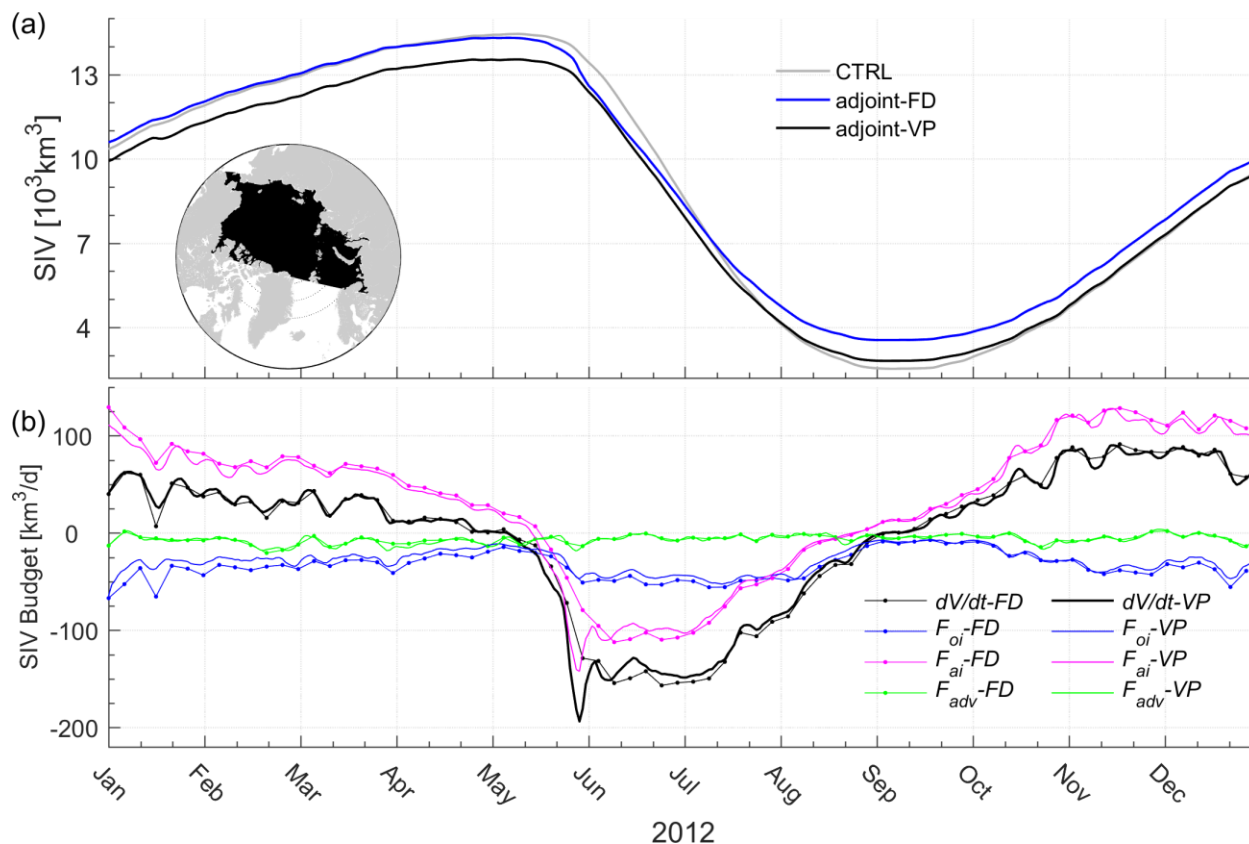
422
423
424   Figure 9. (a) SIV changes in the Arctic Ocean (see the bottom left subplot in Panel (a)) from January to December
425   2012. (b) SIV tendencies and contributions from F_{oi}, F_{ai}, and F_{adv} in adjoint-FD and adjoint-VP (see the legend).
426
427   From May 20 to June 15, the Arctic Ocean observations rely most on satellite-measured SIC. Both the two

428   optimization runs reproduce the observed sea ice extents (SIEs, 15% SIC) well on June 15 (green and red lines in

429   Figure 10a, d), with adjoint-VP slightly better than adjoint-FD in the Barents and Kara Seas (Figure 10a, d).

430   On May 20, adjoint-FD simulates more sea ice than does adjoint-VP (Figure 9a). From May 20 to June 15,

431   adjoint-FD destroys the extra sea ice in the southeastern Beaufort Gyre, the Laptev Sea, the Kara Sea, and north of

432   Svalbard and Franz-Josef-Land through a stronger surface melting F_{ai} (Figure 10b). At the same time, F_{ai} results in

433   less sea ice loss (up to 0.6 m) in adjoint-FD in the central Arctic Ocean. Near the SIMs, F_{adv} differences determine the

434   mean SIT differences (Figure 10a, c). In contrast, mean SIT differences from May 20 to June 15 between adjoint-VP

435   and the control run (Figure 10d) are mostly caused by F_{adv} differences (Figure 10f) and F_{ai} differences have little

436   contribution (Figure 10e), indicating that adjoint-VP modifies the SID to improve the model simulation during this

437   period.

438
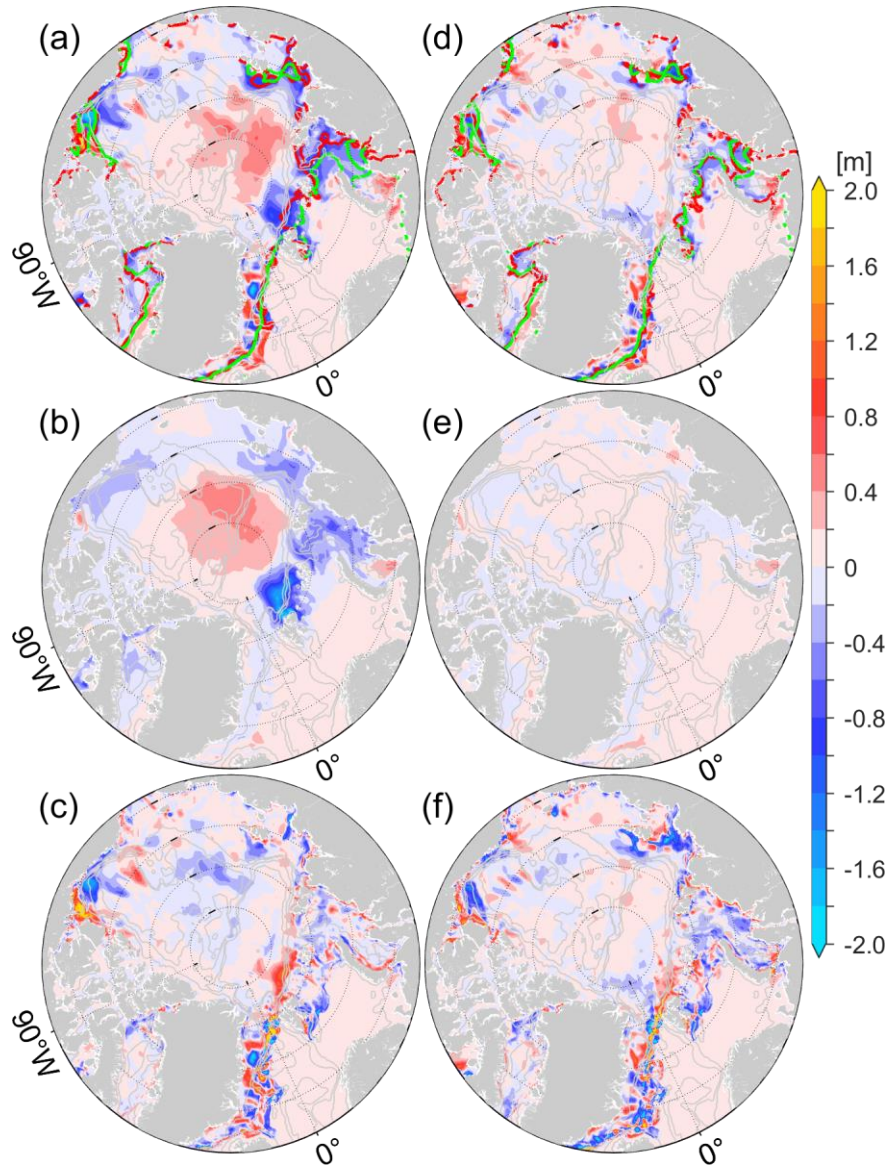
Figure 10. (a) Differences in $\int \frac{dh}{dt}$ integrated from May 20 to June 15 between adjoint-FD and the control run (adjoint-FD minus the control run), attributed to (b) $\int F_{ai}$ and (c) $\int F_{adv}$ differences. Panels (c)-(f) are the same as Panels (a)-(c) but for adjoint-VP. The red and green lines in Panels (a) and (d) indicate the model-simulated (a for adjoint-FD; d for adjoint-VP) and satellite-observed SIEs on June 15.

From May 20 to June 15, the significant sea surface melting anomalies (Figure 10b) are mainly caused by 2-m air temperature adjustments in adjoint-FD (Figure 11a). As shown, the 2-m air temperature is increased by more than 8 ℃ in the marginal seas (prior air temperature uncertainties are ~2-5 ℃) to facilitate the intense surface melting. In the central Arctic Ocean, the 2-m air temperature is reduced by -6 ℃ (Figure 11a), resulting in less sea ice loss up to 0.6 m (Figure 10b) than in the control run. In contrast, adjoint-VP adjusts the 2-m air temperature within ±3 ℃ in the marginal seas (Figure 10b), and the adjustments have little impact on the sea ice surface melting anomalies (Figure 10e). The 2-m air temperature differences averaged from May 20 to June 15 between the ERA5 and NCEP-RA1 reanalyses are within ±3 ℃ (Figure 11c), indicating that adjoint-FD over-adjusts the 2-m air temperature to destroy

452 the extra sea ice. Again, the spatial patterns 2-m air temperature adjustments in adjoint-FD and adjoint-VP don't

453 resemble that of ERA5-NECP differences.

454
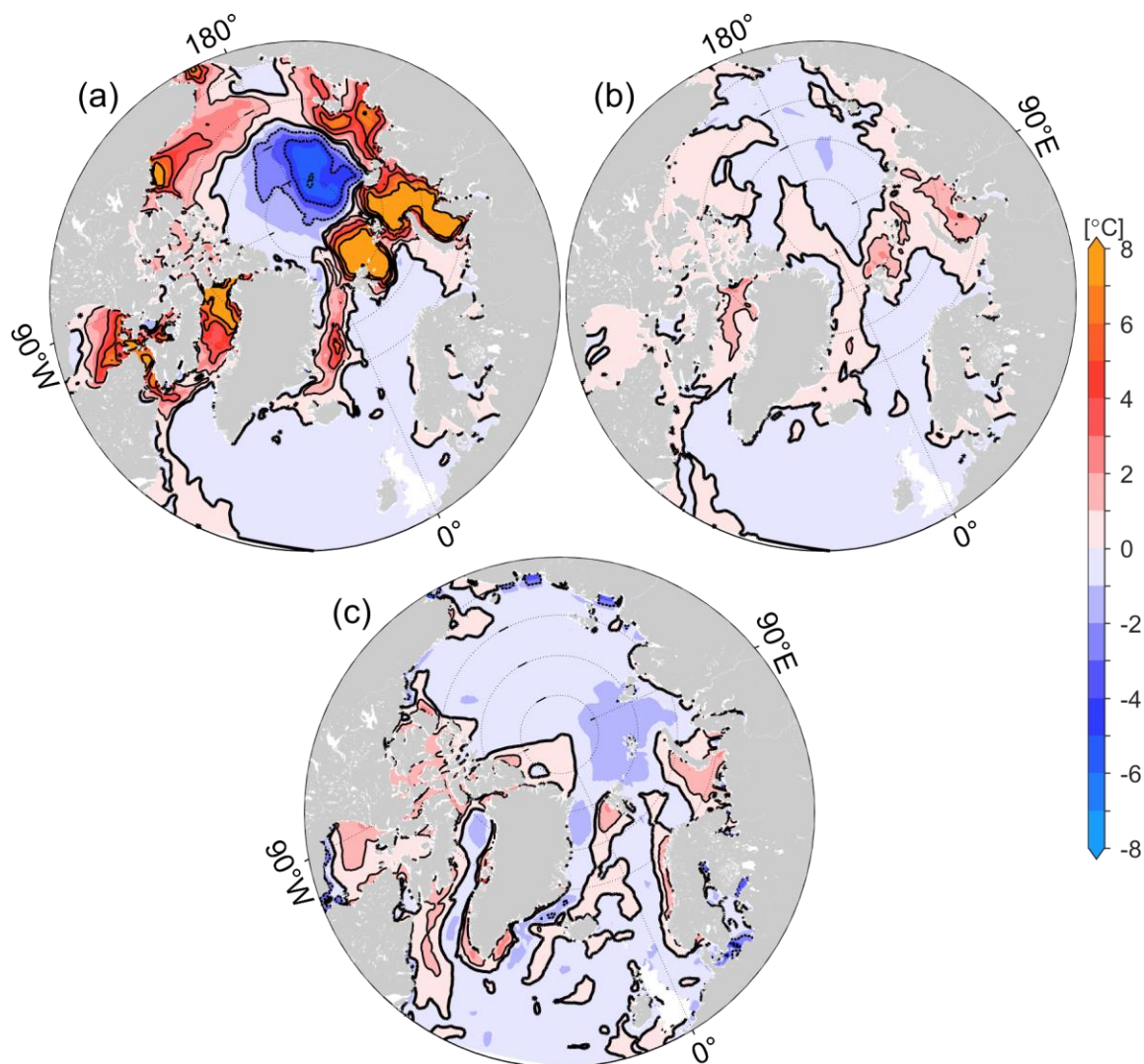
455

456 Figure 11. Adjustments of the 2-m air temperature averaged from May 20 to June 15, 2012, in (a) adjoint-FD and (b)
457 adjoint-VP. Panel (c) shows the 2-m air temperature differences between the ERA5 and NCEP-RA1 reanalyses
458 (ERA5 minus NCEP-RA1) averaged from May 20 to June 15, 2012.

459

460   In summary, the two optimisation runs successfully reproduce the sea ice retreat process in 2012 by assimilating

461 satellite and in situ measurements. However, the sea ice retreat processes differ in the two optimised simulations,

462 especially from May to June, when Arctic Ocean observations rely mostly on satellite-measured SIC. Considering the

463 amplitude of the 2-m air temperature adjustments, the adjustments of the control variables in adjoint-VP are more

464 reasonable than those in adjoint-FD due to the inclusion of the approximate adjoint of sea ice rheology.

6 Conclusions

The adjoint model is a powerful way to calculate the sensitivities of a target function to model variables and has been applied to coupled Arctic ocean and sea ice models for sensitivity studies (Heimbach et al., 2010; Kauker et al., 2009; Koldunov et al., 2013) and state estimations (Fenty and Heimbach, 2013; Koldunov et al., 2017; Lyu et al., 2021b; Nguyen et al., 2021). However, due to the persistent instability issues, the adjoint of sea ice dynamics is traditionally excluded or simplified to the adjoint of a free-drift sea ice dynamic, which potentially hampers the accuracy of the coupled ocean and sea ice estimation.

Based on the study of Toyoda et al. (2019) and the coupled ocean and sea ice modelling and adjoint assimilation system (Lyu et al., 2021a), we approximate the adjoint of a viscous-plastic sea ice dynamic and test the impacts on estimating the spatiotemporal variations in the Arctic ocean and sea ice state.

Two optimisations are performed, one including and one excluding the adjoint of sea ice rheology. Both assimilation exepriments reduce SIC and SIT errors and reproduce the sea ice retreat well. With the improved SIC retreat processes, adjoint-FD and adjoint-VP also show similar ocean temperature changes in the marginal seas and the southern Beaufort Gyre, as solar radiation heats the open water quickly as the sea ice retreats. With the improved adjoint of sea ice dynamics, adjoint-VP allows much stronger adjustments of the initial temperature, resulting in a more significant improvement on the temperature in the North Atlantic Ocean and the intermediate layer (50-700 m) of the Arctic Ocean.

Although that adjoint-FD computes much stronger sensitivities of the cost function to the wind vectors than does adjoint-VP, we note that adjoint-FD adjusts more (less) of the 2-m air temperature (wind vectors) than does adjoint-VP. It is evident that the adjoint sensitivities of wind vectors in adjoint-FD less efficiently reduce the cost function than those in adjoint-VP during the optimisation. Adjoint-FD strongly adjusts the 2-m air temperature to reduce the model-data misfits while adjoint-VP slightly adjusts all the control variables to improve the model simulation.

Using sea ice budget analysis, we further examine the sea ice retreat processes in adjoint-FD and adjoint-VP. We note that adjoint-FD and adjoint-VP show different sea ice thinning processes from May 20 to June 15 and in the marginal seas. Adjoint-FD destroys the extra sea ice in the marginal seas by substantially increasing the 2-m air temperature (up to 8 ℃), which is much larger than the ERA5-NCEP differences. In adjoint-VP, the sea ice thinning is moderate with more reasonable adjustments of 2-m air temperature (within ±3 ℃) and the size of the adjustments are much smaller than the ERA5-NCEP differences. Therefore, by including the adjoint of sea ice rheology, adjoint-VP projects the model-data misfits more properly to the control variables than that in adjoint-FD.

Parameter uncertainties significantly impact ocean and sea ice simulations (Lu et al., 2021; Massonnet et al., 2014; Sumata et al., 2019), and a lack of direct observations of key parameters potentially results in biases in the model simulations and predictions. The development of the adjoint of the viscous-plastic sea ice dynamics further introduces three parameters, including the ice compressive strength constant (P^*), ice strength decay constant (C^*),

498 and ratio of normal stress to shear stress (*e*), into the adjoint model. Since it remains unclear how well the tangent

499 linear approximation could represent the relations between the model parameters and the model state, in the future

500 studies, we will examine the accuracy of the adjoint sensitivities with respect to the model parameters and then further

501 improve the ocean-sea ice estimations by jointly estimating the state and parameters.

7 Data availability

503 The data used to create the plots in the paper are available at Pangaea (https://issues.pangaea.de/browse/PDI-33039).

504 Assimilated observations are listed in Table 1; and the up-looking sonar observed sea ice draft are from the Beaufort

505 Gyre Exploration Project (BGEP, https://www2.whoi.edu/site/beaufortgyre/).

506

507 *Author contribution.* G. Lyu designed the experiments, conducted the experiments and analysis. A. Koehl contributed

508 to the experiment design and interpretations. G. Lyu wrote the first draft. A. Koehl, D. Stammer, X. Wu, and M. Zhou

509 contributed to reviewing and editing the manuscript.

510

511 *Competing interests.* The authors declare that they have no conflict of interest.

512

Acknowledgments

514 This work was funded partly by the Open Fund Project of Key Laboratory of Marine Environmental Information

515 Technology, Ministry of Natural Resources of the People's Republic of China to G. Lyu and by the Shanghai Frontiers

516 Science Center of Polar Science (SCOPS) to M. Zhou. We thank NCEP and ECMWF for offering the NCEP/NCAR-

517 RA1 and ERA5 reanalyses. Thanks to ICDC at University of Hamburg and Alfred Wegener Institute for supplying

518 the ASI-SSM/I sea ice concentration and CryoSat-2/SMOS L4 datasets. We also acknowledge the Met Office, the

519 Copernicus Marine Service, and the Beaufort Gyre Exploration Project for archiving and sharing the EN4, the along-

520 track SLA , and sea ice draft datasets used in assimilation and independent validation.

521

References

523 AMAP, Arctic Climate Change Update 2021: Key Trends and Impacts. Summary for Policy-makers. Arctic
524 Monitoring and Assessment Programme (AMAP), Tromsø, Norway. 16 pp, 2021.
525 Chevallier, M., Smith, G. C., Dupont, F., Lemieux, J.-F., Forget, G., Fujii, Y., Hernandez, F., Msadek, R., Peterson,
526 K. A., Storto, A., Toyoda, T., Valdivieso, M., Vernieres, G., Zuo, H., Balmaseda, M., Chang, Y.-S., Ferry, N.,
527 Garric, G., Haines, K., Keeley, S., Kovach, R. M., Kuragano, T., Masina, S., Tang, Y., Tsujino, H., and Wang, X.:
528 Intercomparison of the Arctic sea ice cover in global ocean–sea ice reanalyses from the ORA-IP project, Climate
529 Dynamics, 49, 1107-1136, 10.1007/s00382-016-2985-y, 2017.
530 Comiso, J. C., Parkinson, C. L., Gersten, R., and Stock, L.: Accelerated decline in the Arctic sea ice cover,
531 Geophysical Research Letters, 35, 10.1029/2007gl031972, 2008.

532 Fekete, B. M., Vörösmarty, C. J., and Grabs, W.: High-resolution fields of global runoff combining observed river
533 discharge and simulated water balances, Global Biogeochemical Cycles, 16, 15-11-15-10,
534 https://doi.org/10.1029/1999GB001254, 2002.
535 Fenty, I. and Heimbach, P.: Coupled Sea Ice–Ocean-State Estimation in the Labrador Sea and Baffin Bay, Journal of
536 Physical Oceanography, 43, 884-904, 10.1175/jpo-d-12-065.1, 2013.
537 Fenty, I., Menemenlis, D., and Zhang, H.: Global coupled sea ice-ocean state estimation, Climate Dynamics, 49,
538 931-956, 10.1007/s00382-015-2796-6, 2017.
539 Giering, R. and Kaminski, T.: Recipes for adjoint code construction, ACM Transactions on Mathematical Software
540 (TOMS), 24, 437-474, 1998.
541 Gilbert, J. C. and Lemaréchal, C.: The module M1QN3, 2006.
542 Good, S. A., Martin, M. J., and Rayner, N. A.: EN4: Quality controlled ocean temperature and salinity profiles and
543 monthly objective analyses with uncertainty estimates, Journal of Geophysical Research: Oceans, 118, 6704-6716,
544 10.1002/2013jc009067, 2013.
545 Heimbach, P., Menemenlis, D., Losch, M., Campin, J.-M., and Hill, C.: On the formulation of sea-ice models. Part
546 2: Lessons from multi-year adjoint sea-ice export sensitivities through the Canadian Arctic Archipelago, Ocean
547 Modelling, 33, 145-158, https://doi.org/10.1016/j.ocemod.2010.02.002, 2010.
548 Heimbach, P., Fukumori, I., Hill, C. N., Ponte, R. M., Stammer, D., Wunsch, C., Campin, J.-M., Cornuelle, B.,
549 Fenty, I., Forget, G., Köhl, A., Mazloff, M., Menemenlis, D., Nguyen, A. T., Piecuch, C., Trossman, D., Verdy, A.,
550 Wang, O., and Zhang, H.: Putting It All Together: Adding Value to the Global Ocean and Climate Observing
551 Systems With Complete Self-Consistent Ocean State and Parameter Estimates, Frontiers in Marine Science, 6,
552 10.3389/fmars.2019.00055, 2019.
553 Hersbach, H., Bell, B., Berrisford, P., Hirahara, S., Horányi, A., Muñoz-Sabater, J., Nicolas, J., Peubey, C., Radu,
554 R., Schepers, D., Simmons, A., Soci, C., Abdalla, S., Abellan, X., Balsamo, G., Bechtold, P., Biavati, G., Bidlot, J.,
555 Bonavita, M., De Chiara, G., Dahlgren, P., Dee, D., Diamantakis, M., Dragani, R., Flemming, J., Forbes, R.,
556 Fuentes, M., Geer, A., Haimberger, L., Healy, S., Hogan, R. J., Hólm, E., Janisková, M., Keeley, S., Laloyaux, P.,
557 Lopez, P., Lupu, C., Radnoti, G., de Rosnay, P., Rozum, I., Vamborg, F., Villaume, S., and Thépaut, J.-N.: The
558 ERA5 global reanalysis, Quarterly Journal of the Royal Meteorological Society, 146, 1999-2049,
559 https://doi.org/10.1002/qj.3803, 2020.
560 Hibler, W.: A Dynamic Thermodynamic Sea Ice Model, Journal of Physical Oceanography, 9, 815-846,
561 10.1175/1520-0485(1979)009<0815:adtsim>2.0.co;2, 1979.
562 Kaleschke, L., Lüpkes, C., Vihma, T., Haarpaintner, J., Bochert, A., Hartmann, J., and Heygster, G.: SSM/I Sea Ice
563 Remote Sensing for Mesoscale Ocean-Atmosphere Interaction Analysis, Canadian Journal of Remote Sensing, 27,
564 526-537, 10.1080/07038992.2001.10854892, 2001.
565 Kalnay, E., Kanamitsu, M., Kistler, R., Collins, W., Deaven, D., Gandin, L., Iredell, M., Saha, S., White, G.,
566 Woollen, J., Zhu, Y., Chelliah, M., Ebisuzaki, W., Higgins, W., Janowiak, J., Mo, K. C., Ropelewski, C., Wang, J.,
567 Leetmaa, A., Reynolds, R., Jenne, R., and Joseph, D.: The NCEP/NCAR 40-Year Reanalysis Project, Bulletin of the
568 American Meteorological Society, 77, 437-472, 10.1175/1520-0477(1996)077<0437:tnyrp>2.0.co;2, 1996.
569 Kauker, F., Kaminski, T., Karcher, M., Giering, R., Gerdes, R., and Voßbeck, M.: Adjoint analysis of the 2007 all
570 time Arctic sea-ice minimum, Geophysical Research Letters, 36, 10.1029/2008gl036323, 2009.
571 Koldunov, N. V., Köhl, A., and Stammer, D.: Properties of adjoint sea ice sensitivities to atmospheric forcing and
572 implications for the causes of the long term trend of Arctic sea ice, Climate dynamics, 41, 227-241, 2013.
573 Koldunov, N. V., Köhl, A., Serra, N., and Stammer, D.: Sea ice assimilation into a coupled ocean–sea ice model
574 usingi ts adjoint, The Cryosphere, 11, 2265-2281, 10.5194/tc-11-2265-2017, 2017.
575 Kwok, R.: Arctic sea ice thickness, volume, and multiyear ice coverage: losses and coupled variability (1958–2018),
576 Environmental Research Letters, 13, 105005, 10.1088/1748-9326/aae3ec, 2018.
577 Large, W. G., McWilliams, J. C., and Doney, S. C.: Oceanic vertical mixing: A review and a model with a nonlocal
578 boundary layer parameterization, Reviews of Geophysics, 32, 363-403, 1994.
579 Large, W. G., and Yeager S.: Diurnal to decadal global forcing for ocean and sea-ice models: The datasets and flux
580 climatologies. NCAR Tech. Note NCAR/TN-4601STR, 105 pp, 2004.
581 Lavergne, T., Sørensen, A. M., Kern, S., Tonboe, R., Notz, D., Aaboe, S., Bell, L., Dybkjær, G., Eastwood, S.,
582 Gabarro, C., Heygster, G., Killie, M. A., Brandt Kreiner, M., Lavelle, J., Saldo, R., Sandven, S., and Pedersen, L. T.:
583 Version 2 of the EUMETSAT OSI SAF and ESA CCI sea-ice concentration climate data records, The Cryosphere,
584 13, 49-78, 10.5194/tc-13-49-2019, 2019.
585 Lindsay, R. W. and Zhang, J.: Assimilation of Ice Concentration in an Ice–Ocean Model, Journal of Atmospheric
586 and Oceanic Technology, 23, 742-749, 10.1175/jtech1871.1, 2006.

Liu, C., Köhl, A., and Stammer, D.: Adjoint-Based Estimation of Eddy-Induced Tracer Mixing Parameters in the Global Ocean, Journal of Physical Oceanography, 42, 1186-1206, 10.1175/jpo-d-11-0162.1, 2012.

Losch, M., Menemenlis, D., Campin, J.-M., Heimbach, P., and Hill, C.: On the formulation of sea-ice models. Part 1: Effects of different solver implementations and parameterizations, Ocean Modelling, 33, 129-144, 2010.

Lyu, G., Koehl, A., Serra, N., and Stammer, D.: Assessing the current and future Arctic Ocean observing system with observing system simulating experiments, Quarterly Journal of the Royal Meteorological Society, 147, 2670-2690, https://doi.org/10.1002/qj.4044, 2021a.

Lyu, G., Koehl, A., Serra, N., Stammer, D., and Xie, J.: Arctic ocean–sea ice reanalysis for the period 2007–2016 using the adjoint method, Quarterly Journal of the Royal Meteorological Society, 147, 1908-1929, https://doi.org/10.1002/qj.4002, 2021b.

Ma, X., Mu, M., Dai, G., Han, Z., Li, C., and Jiang, Z.: Influence of Arctic Sea Ice Concentration on Extended-Range Prediction of Strong and Long-Lasting Ural Blocking Events in Winter, Journal of Geophysical Research: Atmospheres, 127, e2021JD036282, https://doi.org/10.1029/2021JD036282, 2022.

Marshall, J., Adcroft, A., Hill, C., Perelman, L., and Heisey, C.: A finite‐volume, incompressible Navier Stokes model for studies of the ocean on parallel computers, Journal of Geophysical Research: Oceans, 102, 5753-5766, 1997.

Maykut, G. A. and McPhee, M. G.: Solar heating of the Arctic mixed layer, Journal of Geophysical Research: Oceans, 100, 24691-24703, 10.1029/95jc02554, 1995.

Morison, J., Wahr, J., Kwok, R., and Peralta‐Ferriz, C.: Recent trends in Arctic Ocean mass distribution revealed by GRACE, Geophysical Research Letters, 34, 2007.

Mu, L., Losch, M., Yang, Q., Ricker, R., Losa, S. N., and Nerger, L.: Arctic-Wide Sea Ice Thickness Estimates From Combining Satellite Remote Sensing Data and a Dynamic Ice-Ocean Model with Data Assimilation During the CryoSat-2 Period, Journal of Geophysical Research: Oceans, 123, 7763-7780, https://doi.org/10.1029/2018JC014316, 2018.

Nguyen, A. T., Pillar, H., Ocaña, V., Bigdeli, A., Smith, T. A., and Heimbach, P.: The Arctic Subpolar Gyre sTate Estimate: Description and Assessment of a Data-Constrained, Dynamically Consistent Ocean-Sea Ice Estimate for 2002–2017, Journal of Advances in Modeling Earth Systems, 13, e2020MS002398, https://doi.org/10.1029/2020MS002398, 2021.

Overland, J. E., Ballinger, T. J., Cohen, J., Francis, J. A., Hanna, E., Jaiser, R., Kim, B. M., Kim, S. J., Ukita, J., Vihma, T., Wang, M., and Zhang, X.: How do intermittency and simultaneous processes obfuscate the Arctic influence on midlatitude winter extreme weather events?, Environmental Research Letters, 16, 043002, 10.1088/1748-9326/abdb5d, 2021.

Polyakov, I. V., Pnyushkov, A. V., Alkire, M. B., Ashik, I. M., Baumann, T. M., Carmack, E. C., Goszczko, I., Guthrie, J., Ivanov, V. V., Kanzow, T., Krishfield, R., Kwok, R., Sundfjord, A., Morison, J., Rember, R., and Yulin, A.: Greater role for Atlantic inflows on sea-ice loss in the Eurasian Basin of the Arctic Ocean, Science, 356, 285-291, 10.1126/science.aai8204, 2017.

Proshutinsky, A., Krishfield, R., Timmermans, M.-L., Toole, J., Carmack, E., McLaughlin, F., Williams, W. J., Zimmermann, S., Itoh, M., and Shimada, K.: Beaufort Gyre freshwater reservoir: State and variability from observations, Journal of Geophysical Research: Oceans, 114, 10.1029/2008jc005104, 2009.

Proshutinsky, A., Krishfield, R., Toole, J. M., Timmermans, M.-L., Williams, W., Zimmermann, S., Yamamoto-Kawai, M., Armitage, T. W. K., Dukhovskoy, D., Golubeva, E., Manucharyan, G. E., Platov, G., Watanabe, E., Kikuchi, T., Nishino, S., Itoh, M., Kang, S.-H., Cho, K.-H., Tateyama, K., and Zhao, J.: Analysis of the Beaufort Gyre Freshwater Content in 2003–2018, Journal of Geophysical Research: Oceans, 124, 9658-9689, 10.1029/2019jc015281, 2019.

Quadfasel, D., SY, A., WELLS, D., and TUNIK, A.: Warming in the Arctic, Nature, 350, 385, 1991.

Ricker, R., Hendricks, S., Kaleschke, L., Tian-Kunze, X., King, J., and Haas, C.: A weekly Arctic sea-ice thickness data record from merged CryoSat-2 and SMOS satellite data, The Cryosphere, 11, 1607-1623, 10.5194/tc-11-1607-2017, 2017.

Sakov, P., Counillon, F., Bertino, L., Lisæter, K. A., Oke, P. R., and Korablev, A.: TOPAZ4: an ocean-sea ice data assimilation system for the North Atlantic and Arctic, Ocean Sci., 8, 633-656, 10.5194/os-8-633-2012, 2012.

Schauer, U., Beszczynska-Möller, A., Walczowski, W., Fahrbach, E., Piechura, J., and Hansen, E.: Variation of measured heat flow through the Fram Strait between 1997 and 2006, in: Arctic–Subarctic Ocean Fluxes, Springer, 65-85, 2008.

Serra, N., Käse, R. H., Köhl, A., Stammer, D., and Quadfasel, D.: On the low-frequency phase relation between the Denmark Strait and the Faroe-Bank Channel overflows, Tellus A: Dynamic Meteorology and Oceanography, 62, 530-550, 10.1111/j.1600-0870.2009.00445.x, 2010.

643 Smith, W. H. F. and Sandwell, D. T.: Global Sea Floor Topography from Satellite Altimetry and Ship Depth
644 Soundings, Science, 277, 1956-1962, 10.1126/science.277.5334.1956, 1997.
645 Spreen, G., Kaleschke, L., and Heygster, G.: Sea ice remote sensing using AMSR-E 89-GHz channels, Journal of
646 Geophysical Research: Oceans, 113, 10.1029/2005jc003384, 2008.
647 Stammer, D., Wunsch, C., Giering, R., Eckert, C., Heimbach, P., Marotzke, J., Adcroft, A., Hill, C. N., and
648 Marshall, J.: Global ocean circulation during 1992–1997, estimated from ocean observations and a general
649 circulation model, Journal of Geophysical Research: Oceans, 107, 1-1-1-27, https://doi.org/10.1029/2001JC000888,
650 2002.
651 Tilling, R. L., Ridout, A., and Shepherd, A.: Estimating Arctic sea ice thickness and volume using CryoSat-2 radar
652 altimeter data, Advances in Space Research, 62, 1203-1225, https://doi.org/10.1016/j.asr.2017.10.051, 2018.
653 Toyoda, T., Hirose, N., Urakawa, L. S., Tsujino, H., Nakano, H., Usui, N., Fujii, Y., Sakamoto, K., and Yamanaka,
654 G.: Effects of Inclusion of Adjoint Sea Ice Rheology on Backward Sensitivity Evolution Examined Using an Adjoint
655 Ocean–Sea Ice Model, Monthly Weather Review, 147, 2145-2162, 10.1175/mwr-d-18-0198.1, 2019.
656 Uotila, P., Goosse, H., Haines, K., Chevallier, M., Barthélemy, A., Bricaud, C., Carton, J., Fučkar, N., Garric, G.,
657 Iovino, D., Kauker, F., Korhonen, M., Lien, V. S., Marnela, M., Massonnet, F., Mignac, D., Peterson, K. A.,
658 Sadikni, R., Shi, L., Tietsche, S., Toyoda, T., Xie, J., and Zhang, Z.: An assessment of ten ocean reanalyses in the
659 polar regions, Climate Dynamics, 52, 1613-1650, 10.1007/s00382-018-4242-z, 2019.
660 Woodgate, R. A., Weingartner, T. J., and Lindsay, R.: Observed increases in Bering Strait oceanic fluxes from the
661 Pacific to the Arctic from 2001 to 2011 and their impacts on the Arctic Ocean water column, Geophysical Research
662 Letters, 39, 2012.
663 Wunsch, C. and Heimbach, P.: Practical global oceanic state estimation, Physica D: Nonlinear Phenomena, 230,
664 197-208, https://doi.org/10.1016/j.physd.2006.09.040, 2007.
665 Yang, C.-Y., Liu, J., and Xu, S.: Seasonal Arctic Sea Ice Prediction Using a Newly Developed Fully Coupled
666 Regional Model With the Assimilation of Satellite Sea Ice Observations, Journal of Advances in Modeling Earth
667 Systems, 12, e2019MS001938, https://doi.org/10.1029/2019MS001938, 2020.
668 Zhang, J. and Hibler , W.: On an efficient numerical method for modeling sea ice dynamics, Journal of Geophysical
669 Research: Oceans, 102, 8691-8702, 1997.
670 Zhang, J. and Rothrock, D. A.: Modeling Arctic sea ice with an efficient plastic solution, Journal of Geophysical
671 Research: Oceans, 105, 3325-3338, 2000.
672 Zweng, M. M., Reagan, J. R., Seidov, D., Boyer, T. P., Locarnini, R. A., Garcia, H. E., Mishonov, A. V., Baranova,
673 O. K., Weathers, K. W., Paver, C. R., and V, S. I.: World Ocean Atlas 2018, Volume 2: Salinity S, Levitus, edited
674 by: Mishonov, A., NOAA Atlas NESDIS, 82, 50, 2018.
675